Atomic layer deposition of NiO applied in a monolithic perovskite/PERC tandem cell

Solar Energy Materials & Solar Cells 261 (2023) 112498

Contents lists available at ScienceDirect

Solar Energy Materials and Solar Cells

journal homepage: www.elsevier.com/locate/solmat

Atomic layer deposition of NiO applied in a monolithic perovskite/PERC tandem cell

Nga Phung [a,1], Dong Zhang [b,**,1], Cristian van Helvoirt [a], Michael Verhage [a], Marcel Verheijen [a], Valerio Zardetto [b], Frennie Bens [c], Christ H.L. Weijtens [d], L.J (Bart) Geerligs [e], W.M.M. Kessels [a], Bart Macco [a], Mariadriana Creatore [a,f,*]

[a] Department of Applied Physics and Science Education, Eindhoven University of Technology, P.O. Box 513, 5600, MB, Eindhoven, the Netherlands
[b] TNO Partner in Solliance, High Tech Campus 21, Eindhoven, 5656, AE, the Netherlands
[c] TNO/Holst Centre, High Tech Campus 31, Eindhoven, 5656, AE, the Netherlands
[d] Molecular Materials and Nanosystems and Institute of Complex Molecular Systems, Eindhoven University of Technology, P.O. Box 513, 5600, MB, Eindhoven, the Netherlands
[e] TNO, Westerduinweg 3 1755, LE, Petten, the Netherlands
[f] Eindhoven Institute for Renewable Energy Systems (EIRES), PO Box 513, 5600, MB, Eindhoven, the Netherlands

ARTICLE INFO

Keywords:
Perovskite/Silicon tandem cell
Nickel oxide
Atomic layer deposition
PERC
Self-assembled monolayer
Tunnel recombination junction

ABSTRACT

Monolithic perovskite/silicon tandem photovoltaics have fueled major research efforts as well as gaining rapid industrial interest. So far, most of the literature has focused on the use of currently more expensive silicon heterojunction bottom cell technology. This work demonstrates a perovskite/silicon tandem solar cell based on the industrially dominant passivated emitter and rear cell (PERC) technology. In detail, we investigate a tunnel recombination junction (TRJ) consisting of ITO/NiO/2-(9*H*-carbazol-9-yl)ethyl] phosphonic acid (2PACz) and compare it with an ITO/2PACz TRJ. Specifically, the NiO layer is deposited by atomic layer deposition (ALD). Although ITO/2PACz-based tandem devices can reach more than 24% conversion efficiency, we observe that they suffer from a large spread in photovoltaic parameters due to electrical shunts in the perovskite top cell, caused by the inhomogeneity of the 2PACz layer on ITO. Instead, when ALD NiO is sandwiched between 2PACz and ITO, the surface coverage of 2PACz improves and the yield of the devices, in terms of all device parameters, also improves, *i.e.*, the standard deviation decreases from 4.6% with ITO/2PACz to 2.0% with ITO/NiO/2PACz. In conclusion, thanks to the presence of NiO, the TRJ consisting of ITO/NiO/2PACz leads to a 23.7% efficient tandem device with narrow device efficiency distribution.

1. Introduction

Tandem photovoltaics (PV) based on metal halide perovskite and crystalline silicon solar cells has attracted major research efforts due to its perspective to be cost-effective and to accelerate the solar energy deployment to fulfill the net zero emission target in 2050 [1]. This is primarily to be attributed to the high efficiency and estimated low cost production of the perovskite technology, combined with mass produced silicon PV. The tandem perovskite/silicon cell is predicted to deliver electricity at lower costs than silicon PV only [2]. The field of perovskite/silicon tandem photovoltaics has rapidly advanced and has recently reached 33.7% conversion efficiency [3]. However, these tandem records generally adopt the currently more expensive silicon heterojunction (SHJ) technology [4]. In fact, SHJ is very commonly used as bottom cell in perovskite/silicon tandem. The likely reason is that SHJ cells employ transparent conductive oxide (TCO) as electrodes, making the integration of the perovskite top cell rather straightforward in a monolithic tandem since the TCO then serves as one of the layers for the tunnel recombination junction (TRJ). In contrast, the use of other silicon PV technologies namely Al-BSF (back surface field), PERT/PERL

* Corresponding author. Department of Applied Physics and Science Education, Eindhoven University of Technology, P.O. Box 513, 5600, MB, Eindhoven, the Netherlands.
** Corresponding author.
E-mail addresses: dongzhangdz@gmail.com (D. Zhang), m.creatore@tue.nl (M. Creatore).
[1] These authors contributed equally to the work.

https://doi.org/10.1016/j.solmat.2023.112498
Received 24 February 2023; Received in revised form 9 July 2023; Accepted 4 August 2023
Available online 18 August 2023

(passivated emitter rear totally diffused/passivated emitter with rear locally diffused), PERC (passivated emitter and rear cell), and TOPCon (tunneling oxide passivated contact) cells in monolithic perovskite/silicon tandem solar cells is rather limited in literature. Here, we summarize the literature overview on monolithic perovskite/silicon tandems based on those bottom cells in Fig. 1 and Table S1. The highest tandem efficiencies have been achieved with TOPCon-like bottom cells [5,6] due to the lower open circuit voltage (V_{OC}) of PER-X-based tandem compared to the TOPCon-based counterpart. This is because the V_{OC} of TOPCon-like bottom cells with polycrystalline silicon (poly-Si) on the front side can be largely retained in the presence of the tunnel oxide and polycrystalline silicon layer (schematic in Fig. S1a) [6–8]. Note that the highest efficiency of 28.7% in Fig. 1 is with a monolithic perovskite/silicon based on a TOPCon-like bottom cell [5]. Instead, for integration of a standard PER-X in a monolithic tandem cell, the dielectric surface passivation layers cannot be present at the front of the bottom cell. As a consequence, the PER-X bottom cell has a large V_{OC} loss due to the direct contact between the TRJ and silicon, resulting in a relatively low V_{OC} of the tandem cell [9]. The approach in the present study is to use a standard architecture of PERC silicon cell as the bottom cell with n^+ diffused junction in the front side (Fig. S1b). We chose PERC as bottom cell in this study because it would be certainly appealing also from an industrial point of view. PERC technology has reached a market share of close to 80% in 2020, thereby being one of the work horses for the silicon PV technology [10]. Thus, in order to accelerate the advancement of tandem perovskite/silicon towards its maturity and keeping the cost low, it could be strategic to adopt the industrial standard PERC as bottom cell for easy integration of perovskite PV processing in the production line of current silicon technology.

To realize the potential of PERC/perovskite tandem solar cell, the optimization of TRJ plays an important role. So far, for the state-of-the-art monolithic perovskite/silicon tandem devices, the TRJ includes a TCO layer that collects electrons from the bottom cell, generally indium tin oxide (ITO) or indium zinc oxide (IZO), in combination with a p-type layer, which serves also as hole transport layer (HTL) in the perovskite top cell [21]. Specifically, a TRJ consisting of IZO and self-assembled monolayer (SAM) is employed in the 29.8% perovskite/silicon tandem [22], and ITO/SAM led to a previous record tandem cell of more than 29% efficiency with an SHJ bottom cell [23]. It is generally observed that the application of a SAM boosts the efficiency of the device due to its "lossless" interface with the perovskite absorber [24]. Nonetheless, it has been reported that solution processing of SAM on ITO is strongly affected by the ITO crystallinity and morphology. For example, ITO can have different crystal facets affecting SAM chemisorption and possibly resulting in defective SAM [25]. The surface roughness of ITO also affects the molecular density of SAM processed directly on ITO [26]. Moreover, an ITO surface treatment prior to SAM processing is crucial, *e.g.*, UV-O_3 treatment has been found essential to activate surface sites for SAM chemisorption [24]. Recently, we have shown that a hydroxyl-rich plasma-assisted atomic layer deposited NiO improves the homogeneity of SAM compared to direct SAM processing on ITO in perovskite single junction devices, thereby suppressing electrical shunts in the devices and spread in PV device parameters [27].

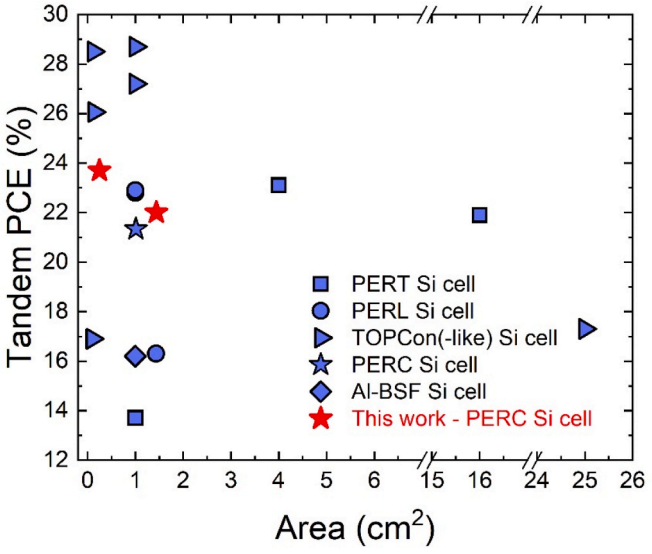

Fig. 1. Literature overview of the conversion efficiency of monolithic perovskite/Si tandem solar cells using homojunction or poly-Si based-silicon bottom cells as a function of the reported device area [6–9], [11–20]. PERT = passivated emitter rear totally diffused cell, PERL = passivated emitter and rear locally diffused cell, TOPCon = tunneling oxide passivated contact silicon cells, PERC = passivated emitter rear cell, Al-BSF consists of a full-area Al back surface field (BSF). Full structure of the different silicon cells can be found in Table S1, Supporting Information.

Therefore, in the present work, we adopt and compare ITO/2PACz (where 2PACz stands for [2-(9*H*-carbazol-9-yl)ethyl]phosphonic acid) SAM and ITO/NiO/2PACz as TRJs for monolithic perovskite/silicon tandem solar cells, based on PERC as the silicon bottom cell. In addition to the device performance, we also investigate the yield of both device stacks. Whereas our previous work on single junction perovskite PV adopted plasma-assisted ALD NiO, in the present study, NiO is synthesized by thermal ALD NiO. We consider the selection of a thermal ALD process as an opportunity for scaling up the NiO process by batch ALD or spatial ALD [28,29]. When applying this ALD NiO in the TRJ, we achieve a 23.7% efficient tandem device with a narrow device distribution (standard deviation of efficiency is 2% compared to ITO/SAM device with 4.6% standard deviation), which is one of the best efficiencies so far reported when adopting the PERC technology as the bottom cell.

The first part of this manuscript will focus on the tandem device performance with ITO/SAM and ITO/NiO/SAM as TRJ. The investigation of the device stack by transmission electron microscopy will be presented. The difference between the tandem device performances is further elucidated by electrostatic force microscopy. Finally, a conclusion and outlook for a pathway to reach more efficient tandem cells based on an industrial PERC bottom cell are reported.

2. Results and discussion

2.1. Tandem device performance

To assess the performance of the two ITO/SAM and ITO/NiO/SAM TRJs, we fabricated monolithic tandem devices with a commercial PERC bottom cell and a p-i-n perovskite top cell. The tandem devices consist of a front chemically polished close-to-industrial-standard PERC bottom cell with a 30 Ω/sq n^+ emitter and a triple cation ($Cs_{0.05}FA_{0.79}MA_{0.16}Pb(I_{0.75}Br_{0.25})_3$) perovskite top cell (where FA is formamidinium and MA is methylammonium). Note that standard commercialized PERC has higher resistivity for the emitter than in this study. In addition, we adopt ALD NiO deposited using N,N′-di-tert-butylacetamidinato)Nickel(II) as precursor and H_2O as co-reactant, for which we report the process development in detail and its characterization in the Supporting Information (Figs. S2–S6 together with the detailed discussion in Section 2). Further details on device fabrication can be found in the Method section. Fig. 2 reports the power conversion efficiency (PCE), short circuit current (J_{SC}), open circuit voltage (V_{OC}) and fill factor (FF) of the tandem devices (band alignment between TRJ and perovskite absorber is reported in Fig. S7). As can be seen in Fig. 2a, the ITO/2PACz TRJ leads to a device efficiency as high as 24% (J_{SC} = 18.6 mA/cm^2, V_{OC} = 1.69 V, FF = 76.9%). However, the device efficiency also exhibits a large spread among cells with an average PCE of only 14.4% and a standard deviation of 4.6%. This large spread is observed for all photovoltaic parameters. In particular, the V_{OC} of some devices are below 1 V and accompanied by a low FF (Fig. 2c and d). The

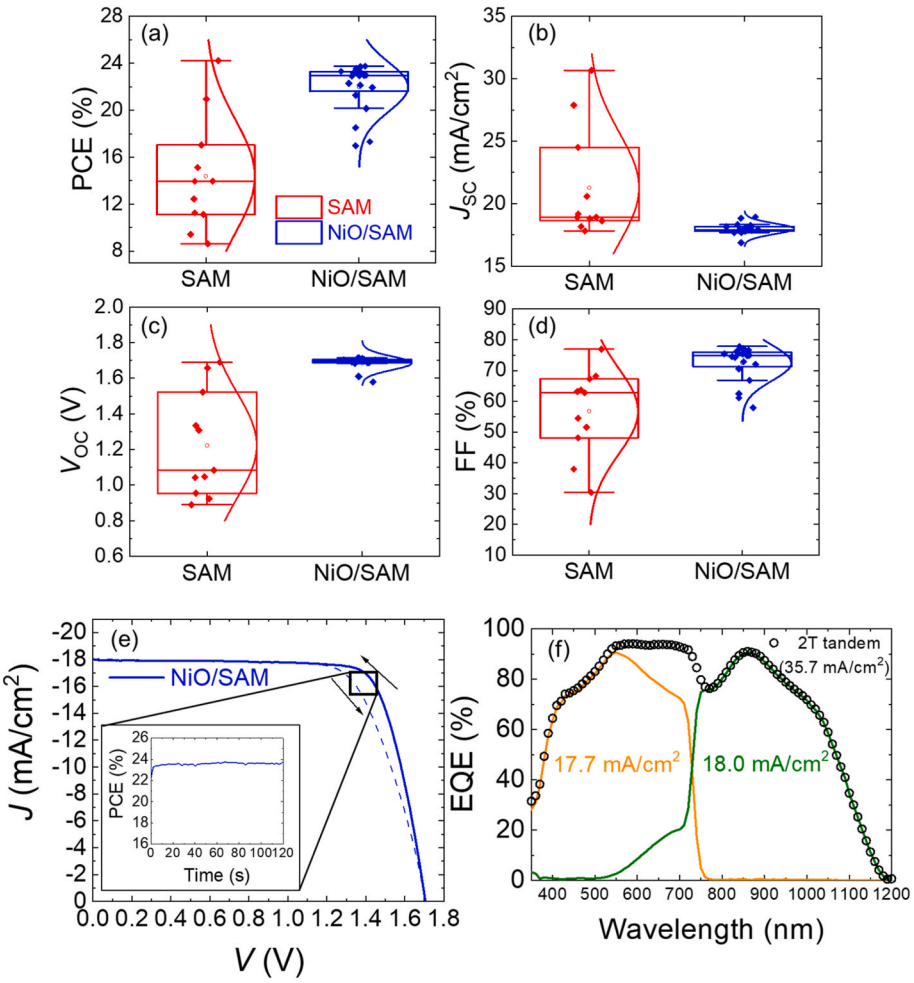

Fig. 2. Box charts of PV parameters of tandem cells (active area of 0.25 cm^2) using different TRJ of ITO/2PACz or ITO/NiO/2PACz: (a) Power conversion efficiency (PCE); (b) Short circuit current (J_{SC}); (c) Open circuit voltage (V_{OC}); (d) Fill factor (FF). The data are collected from reverse *J-V* scan with 133 mV/s scan rate. Box charts represent 25–75%, whiskers are 5%–95%, rest is outliers. Data collected from 31 devices, with 11 ITO/SAM devices and 20 ITO/NiO/SAM devices. (e) *J-V* and (f) EQE of the champion ITO/NiO/SAM tandem cell.

devices with low V_{OC} also exhibit high J_{SC} reaching more than 20 mA/cm^2. This implies that the response of these cells derives mainly from the silicon bottom cell. Fig. S8 (Supporting Information) presents the *J-V* curve of underperforming tandem cell based on ITO/SAM TRJ, with a tilting shape at near J_{SC} indicating that this cell suffers from shunting problems in the top cell. We note that the silicon cell delivers higher current than expected (some cells reached more than 30 mA/cm^2 even with the perovskite layer on top) due to the employed solar simulator's IR peaks (Fig. S9, Supporting Information). This spectral variation does not affect well-performing devices as the perovskite top cell is the current-limiting sub-cell in this case. In contrast, when ALD NiO is introduced between ITO and 2PACz, the spread of the device performance decreases, and the cells operate uniformly across different devices within a batch and from batch-to-batch. Furthermore, Fig. S10 shows that higher shunt resistance is obtained in tandems with NiO compared to those without NiO, which corroborate our hypothesis that ITO/SAM-based tandem has a shunting problem, specifically at the perovskite top cell. The series resistance of ITO/NiO/SAM-tandem cell is higher on average compared to the ITO/SAM-based counterpart. This agrees with the ideality factor and pseudo-FF analysis showing that NiO introduces more transport losses (Fig. S11 and Fig. S12). This observation is in agreement with our previous work on perovskite single junction cell employing a similar SAM chemistry and plasma-assisted ALD NiO, where the variation in ITO/SAM devices performance rooted from the inhomogeneity of SAM development on ITO. On the other hand, the presence of NiO layer induces a homogeneous SAM formation enabling similar device efficiency through device batches [27]. In a later section, more characterization will be reported to elucidate the reason behind the difference between ITO/NiO/SAM-based and ITO/SAM-based tandem cell device efficiency distribution.

Fig. 2e shows the current density – voltage (*J-V*) curve of the best tandem device made with ITO/NiO/SAM TRJ. The cell exhibits a slight hysteresis (forward scan yields a PCE of 21.9% whereas reverse scan yields 23.7%). However, in the maximum power point (MPP) tracking curve for 120 s shown in the inset, the cell efficiency stabilizes at 23.6%, which is very close to the reverse scan efficiency. Fig. 2f shows the external quantum efficiency (EQE) response of the two sub-cells. EQE curves show a very good current match as both cells generate approximately 18 mA/cm^2, which is in excellent agreement with the value reported from *J-V* measurements. We also fabricated a larger 1.44 cm^2 cell with ITO/NiO/SAM TRJ and the quasi-steady-state efficiency of that cell reached 21.9%, as can be seen in the MPP curve shown in Fig. S13 (Supporting Information). That is in line with the average PCE shown in Fig. 2a.

Together with the statistics given in Fig. 2, we report in Table 1 the photovoltaic parameters of the champion tandem and single junction devices. The tandem device reaches 23.7% using ITO/NiO/SAM (J_{SC} = 18.0 mA/cm^2, V_{OC} = 1.705 V, FF = 77.2%) with an average of 22% and a standard deviation of only 2.0% - significantly lower than devices without NiO. Notably, the V_{OC} of devices with ITO/NiO/SAM has a very narrow distribution of an average of 1.68 V (best of 1.705 V). This is very close to the sum of V_{OC} of silicon (without filter) and perovskite single junction cells as can also be seen in Table 1. The low voltage loss of only 50 mV indicates a well-performing TRJ. This amount of voltage loss is on-par with the state-of-the-art tandem perovskite/silicon cells reported in the literature as can be seen in Fig. S14 (Supporting Information).

Table 1
The device parameters of the best single junction cells and tandem cells.

	TCO	HTL	J_{SC} (mA/cm^2)	V_{OC} (V)	FF (%)	PCE (%)
Silicon PERC single-junction	ITO	–	37.2	0.596	74.8	16.6
Perovskite single-junction (semi-transparent cell)	ITO	2PACz	18.3	1.141	80.8	16.9
Perovskite single-junction (semi-transparent cell)	ITO	NiO/2PACz	18.4	1.158	77.9	16.6
2T tandem perovskite/silicon	ITO	2PACz	18.6	1.689	76.9	24.2
2T tandem perovskite/silicon	ITO	NiO/2PACz	18.0	1.705	77.2	23.7

Thus, the tandem device using ITO/NiO/SAM leads to an absolute PCE increase of about 7% in comparison to both single-junction perovskite and silicon cells.

2.2. Transmission electron microscopy analysis of tandem cell using ITO/NiO/SAM

Cross-sectional transmission electron microscopy (TEM) imaging was performed to elucidate the quality of all layers in the perovskite top cell consisting of ITO/NiO/SAM/perovskite/C_{60}/SnO_2/ITO/MgF_2/Ag (Fig. 3a). The perovskite layer is compact and consists of grains extending over the entire thickness of the layer. Here, we also used spatial ALD SnO_2 as buffer layer to protect the perovskite layer from sputter damage during the top TCO electrode deposition. The ALD SnO_2 has been widely used in the perovskite field as an effective protective coating for the perovskite [30]. The SnO_2 is fabricated on a C_{60} layer, which is needed to prevent the direct interaction between the ALD precursor and the perovskite layer that can reduce the device performance, as previously reported [31,32]. Note that due to the roughness of the perovskite, the conformality of the C_{60} layer on perovskite is challenging to be fully captured by TEM. This is because the projected interface roughness yields local blurry interface areas in the image. Finally, the anti-reflection coating layer is applied on the top TCO electrode as 120 nm MgF_2, resulting in excellent current matching as can be seen in Fig. 2f.

We further focus on the interface ITO/NiO/SAM. As can be seen in the high angle annular dark field (HAADF)-STEM image in Fig. 3b, different layers can be discerned by their contrast because the brightness of the image is roughly proportional to Z^2, where Z is the atomic number. Thus, the ITO layer is brighter due to heavy elements (In and Sn). The adjacent darker layer can be assigned to NiO, as also evidenced from the Ni profile displayed in the quantified energy dispersive X-ray (EDX) compositional line profiles in the inset. Although the phosphorus signal is below the detection limit of EDX used in this work, the 2PACz layer can be recognized by the increase in carbon signal (black trace) in proximity to the NiO/perovskite interface. This spike is attributed to the carbon of the SAM rather than to the carbon in the perovskite, if we consider that the onset in the signals of lead and iodine associated to the perovskite layer appears at the right side of the onset in the carbon signal attributed to SAM. The X-ray photoelectron spectroscopy (XPS) investigation corroborates this finding in Fig. 3: in Fig. S4c (Supporting Information) a P2p signal is clearly visible in the NiO/2PACz sample, confirming the presence of SAM on NiO. We estimate from the image in Fig. 3b that the SAM is approximately 1.5–2.5 nm thick. We note that this thickness is larger than the 2PACz molecular length (less than 1 nm) [33], which is similar to what has been observed previously with another phosphonic SAM in our previous work [27].

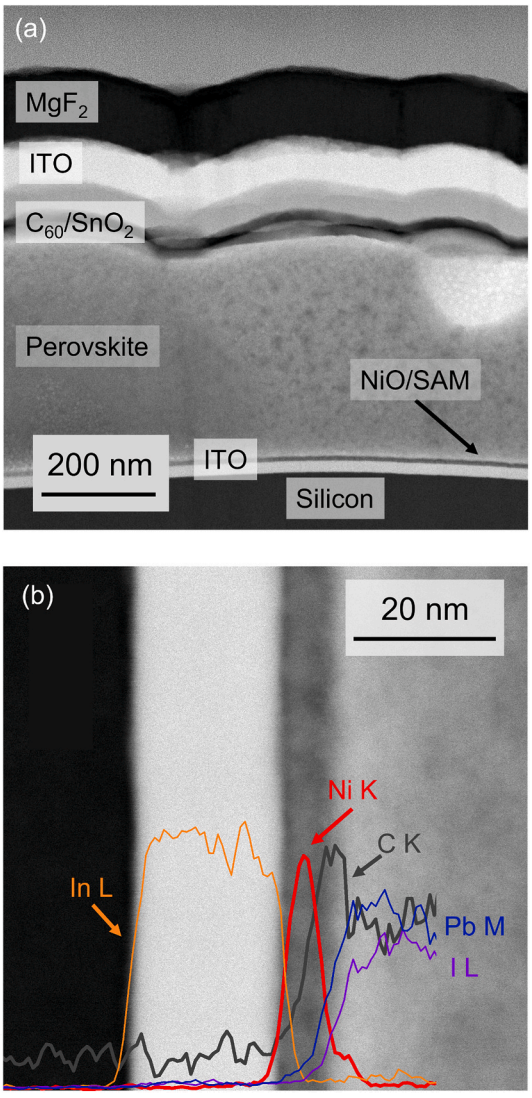

Fig. 3. (a) HAADF-scanning transmission electron microscopy (TEM) image of a tandem cell using ITO/NiO/2PACz. (b) Compositional line profiles at the interface ITO/NiO/SAM extracted from an EDX elemental mapping. Note that the figure is rotated 90°.

2.3. Electrical quality and uniformity of the ITO/(NiO)/SAM interface

The improvement in device yield in the presence of NiO could be attributed to the quality of the HTL/perovskite interface or difference in perovskite formation on two TRJs. Therefore, we investigated the perovskite layers grown on ITO/SAM and ITO/NiO/SAM. We adopted scanning electron microscopy (SEM) and X-ray diffraction (XRD) to investigate the morphology of the perovskite layers deposited on ITO/SAM and ITO/NiO/SAM, as shown in Fig. S15 (in section 3 of the Supporting Information). The SEM analysis of Figs. S15a–b shows no relevant difference in terms of grain size distribution in the perovskite when grown on ITO/SAM and ITO/NiO/SAM (Figs. S15c–d). Interestingly, Li et al. also reported a large number of shunted cells when using only SAM on flexible ITO substrates in all perovskite tandem devices. In contrast, using NiO/SAM significantly improved the device yield, where NiO layer is fabricated by solution-processing from nanoparticles [34]. They attributed this improvement to better wetting of perovskite solution on ITO/NiO/SAM, which delivered a compact perovskite layer, unlike a perovskite film with pinholes, when processed directly on ITO/SAM. Although the improvement in device yield is similar to our case, the SEM image in Fig. S15a shows that the perovskite layer on ITO/SAM is

compact without pinholes, ruling out the difference in perovskite coverage in this study. In addition, Figs. S15e–f reports the XRD patterns of the perovskite layers: there is only a negligible difference in the perovskite crystallographic structure when the absorber is grown on NiO/SAM or on SAM. Hence, we can conclude that the improvement in device yield upon introduction of NiO in the TRJ cannot be attributed to the perovskite microstructure and crystallographic properties.

We then hypothesize that the electrical shunts in the top cell when adopting ITO/SAM as TRJ, as addressed in relation to Fig. 2c and d, are caused by an inhomogeneous distribution of 2PACz on ITO. This has been already observed in perovskite single junction using plasma-assisted ALD NiO [27] and sputtered NiO [35] in combination with phosphonic acid SAM. To verify this hypothesis, we carry out electrostatic force microscopy (EFM) measurements on the ITO/SAM surface. Fig. 4 presents the contact potential difference (CPD) map of the ITO/-SAM. The CPD between the EFM tip and the surface represents the difference in work function between the tip and the material underneath. Thus, it is possible to rely on the relative change in CPD mapping to investigate the homogeneity of the SAM. This is because the work function of 2PACz is 5.2 eV, whereas the work function of the employed ITO is 4.0 eV, and the work function of ALD NiO is 4.3 eV, as measured by ultraviolet photoelectron spectroscopy (see Method for details). As can be seen in Fig. 4a and b, the map shows variation in CPD of the SAM layer deposited on ITO, which is different from the homogeneous CPD of ITO without SAM, despite similar morphology features (height map of ITO and ITO/SAM can be found in Fig. S16, Supporting Information). There are several spots on the map in Fig. 4a showing lower CPD than the rest of the surface of the sample. These low CPD spots likely correspond to exposed ITO areas, as the work function of the ITO is lower than the work function of SAM. It is plausible that the different densities of these spots lead to the difference in perovskite top cell performance, resulting in a large device performance variation seen in Fig. 2c and d. In contrast, when NiO is introduced in the TRJ, the CPD map shows no significant local variation (Fig. 4c), suggesting homogeneous SAM formation and corroborating the TEM results. We attribute this difference in SAM distribution on ITO and ITO/NiO to the higher hydroxyl group density on the NiO surface with respect to pristine ITO, as shown by XPS. The XPS analysis of O1s spectra on ITO/NiO and ITO surfaces in Figs. S4 and S5 (Supporting information) indicates that the NiO surface is characterized by a higher ratio of hydroxyl bonds to metal oxide bonds ($-OH/O^{2-} = 0.66 \pm 0.07$) than the pristine ITO surface ($-OH/O^{2-} = 0.43 \pm 0.04$). A similar observation has been reported for SAM directly deposited on different ITO layers, where ITO layers with a higher hydroxyl concentration result in non-shunted single junction device, whereas sputtered ITO in a monolithic perovskite/SHJ tandem with low -OH concentration results in shunted top cells and thereby non-working tandem cells [36]. Note that the ITO/SAM and ITO/NiO/SAM have similar roughness of 46 and 44 nm, respectively, as extracted from atomic force microscopy height maps in Fig. S16 (Supporting information). This indicates that roughness is not the cause for the difference seen in device efficiency distributions utilizing ITO/SAM or ITO/NiO/SAM.

Furthermore, the average CPD values in Fig. 4d are lower for the ITO/NiO/SAM sample than for the ITO/SAM sample (27 mV and 38 mV, respectively). This variation in CPD value of SAM may arise from the intrinsic sensitivity of the measurement (±3 mV), and a slight difference in SAM formation on the two metal oxides. Literature shows that the SAM surface molecular density or its binding configuration can affect its work function [37,38]. Hence, it confirms the difference in SAM layer distribution when directly deposited on ITO and on ITO/NiO. In conclusion, the EFM analysis shows that the presence of NiO improves the SAM surface homogeneity, most certainly leading to the decrease of electrical shunts of the top cells and thereby enabling highly efficient tandems with a narrower efficiency distribution between cells than those based on the ITO/SAM TRJ. This highlights the benefit of using NiO, as surface treatment is not required before SAM deposition, unlike in ITO case (see Methods for fabrication details). In our opinion, this gives NiO an advantage over ITO or other TCOs because surface

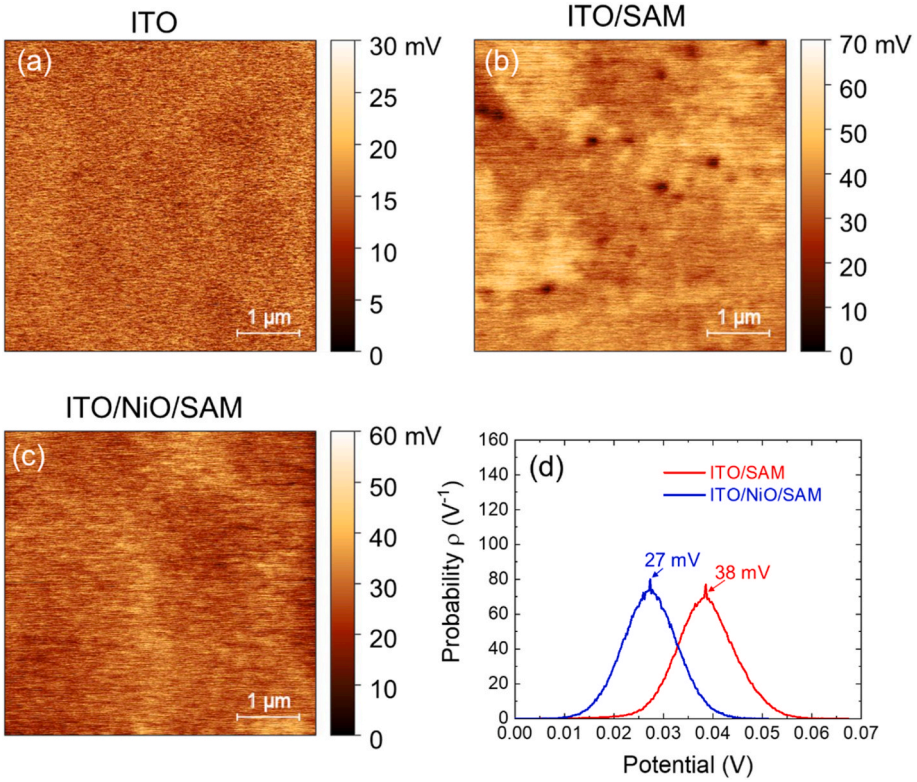

Fig. 4. Electrostatic force microscopy (EFM): Contact potential difference (CPD) of (a) ITO sample. (b) ITO/SAM and (c) ITO/NiO/SAM. The height maps are presented in Fig. S16 in section 4 of the Supporting Information. (d) The statistical distribution of CPD of ITO/SAM and ITO/NiO/SAM.

treatment often requires optimization (roughness, surface chemistry, *etc.*), whereas the intrinsic properties of a film, such as NiO, can be tuned more effectively. Although our study focused on ALD NiO, we expect that other fabrication methods can be adopted, such as sputtering of NiO [39,40].

3. Conclusion and outlook

In this study, we report on a monolithic tandem PV device based on a metal halide perovskite top cell and a close- to- industrial standard PERC bottom cell with ITO/NiO/2PACz SAM as tunnel recombination junction. Although the tandem devices with 2PACz deposited directly on ITO can reach a champion efficiency of 24%, the spread of the device efficiency is quite large with a standard deviation of 4.6%. The latter is primarily visible in V_{OC} and FF, with several cells showing mostly response only from silicon and indicating the presence of electrical shunts in the top cells (V_{OC} is below 1 V). Observation of non-uniformities in CPD maps by EFM analysis strongly suggests that the shunting problem is due to exposed ITO areas, *i.e.*, not covered by SAM. When ALD NiO is introduced between ITO and 2PACz, the yield of the tandem device significantly improves (the standard deviation reduces to 2%), with a champion device of 23.7%. This study shows the benefit of adopting ALD NiO to largely improve the uniformity of coverage of SAM, which is considered beneficial in view of scaling up to larger area tandem PV and, therefore, larger area processing of SAM.

On the roadmap to further improve the efficiency of the device, several directions can be considered. First, light management is desirable to increase the current of the bottom cell. In the present study, the front-side surface of PERC is chemically polished, thus, near-infrared light scattering is not effective, which limits the current generation of the PERC cells. Hence, we expect that a textured front side can improve the achieved J_{SC} of the tandem cells. Furthermore, in the current study the bottom cell front surface is non-passivated, which limits the V_{OC} of the bottom cell. For example, it has demonstrated that alternative TCOs, such as Al-doped ZnO, instead of ITO, can passivate the n^+ -doped surface in silicon solar cells [41] by chemical passivation and field effect passivation [42]. The use of this passivation is expected to increase the V_{OC} and FF of the final tandem device. Hence, with the mentioned viable routes, the efficiency of a perovskite/PERC tandem cell can increase.

4. Method

4.1. Solar cell fabrication

The half-fabricated PERC cell was prepared including a chemical polish of the front side to make a planar substrate for the top cell processing, with a wafer thickness of 180 μm. The n^+ diffused emitter had a sheet resistance of 30 Ω/sq. The received half-fabricated PERC cell was treated with UV-O_3 for cleaning of the emitter surface. Afterwards, a 20 nm indium tin oxide was sputtered using an AJA sputter tool. Substrates of 3x3 cm^2 were cut from the PERC bottom cell for TRJ and perovskite top cell processing, with the area of the top cell being 0.7x0.7 cm^2 or 1.2x1.2 cm^2, defined by the area of the TCO layers and design of front metallization. Prior to NiO deposition, a 15 min O_2 plasma treatment step was carried out to treat the ITO surface. Alternatively, in a device without NiO, the ITO surface was cleaned with UV-O_3 treatment. Note that all substrates are exposed to air for 15 min prior to SAM processing due to sample transfer.

The NiO deposition was carried out in a commercial FlexAL™ MK1 reactor from Oxford Instruments. Both process chamber and loadlock were equipped with a rotary and turbo molecular pumping unit such that base pressure of 10^{-6} Torr could be reached. The process used for solar cells was with 150 °C table temperature and 120 °C chamber temperature. The thickness of NiO used in tandem cells was 8 nm. We note that during the engineering of the NiO layers, its thickness influenced the device spread of perovskite single junction cells. Moreover, considering the transport loss caused by NiO derived from the result of Sun-V_{OC} measurement (Fig. S11 and Fig. S12), increasing further the NiO film thickness was not desirable. The details of the process development of ALD NiO can be found in the Supporting Information. For the SAM solution [2-(9H-carbazol-9-yl)ethyl]phosphonic acid (2PACz) (TCI Chemicals) was used which was dissolved in anhydrous ethanol (Merck Millipore) with 30 min of sonication at a concentration of 0.33 mg/mL.

Prior to the preparation of perovskite precursor solutions, the stock solutions of PbI_2, $PbBr_2$ and CsI were made, stored in the glovebox and repeatedly used. PbI_2 (5532 mg) (TCI Chemicals, 99.99% trace metal basis) was dissolved in a mixture of DMF (7.2 mL) (Sigma Aldrich, 99.8%) and DMSO (0.8 mL) (Sigma Aldrich, 99.9%), $PbBr_2$ (1101 mg) (TCI Chemicals, >98.0%) in a mixture of DMF (1.8 mL) and DMSO (0.2 mL), and CsI (779.4 mg) (Sigma-Aldrich, 99.999% trace metal basis) in DMSO (2 mL). Right before making the perovskite precursor solution, the PbI_2 and $PbBr_2$ stock solutions were heated to 150 °C for 15 min and then cooled to room temperature. The perovskite precursor solution was prepared by mixing formamidinium iodide (FAI) (Greatcell Solar Materials) (283.2 mg), methylammonium bromide (MABr) (Greatcell Solar Materials) (36.88 mg) with PbI_2 stock solution (1077 μL), $PbBr_2$ stock solution (454.3 μL), and CsI stock solution (69.3 μL) to realize the nominal perovskite composition of $Cs_{0.05}FA_{0.79}MA_{0.16}Pb(I_{0.75}Br_{0.25})_3$. All materials were purchased from commercial sources and used as received.

For the electron transport layer, a C_{60} layer was evaporated with a rate of 0.05 nm/s to reach around 20 nm on top of the perovskite. The spatial ALD SnO_2 buffer layer was deposited in a home-built setup using tetrakis(dimethylamino)tin(IV) as the precursor and H_2O as the co-reactant using 500 sccm Ar flow. A nitrogen curtain was used to separate the two half reactions. The deposition process was carried out at a temperature of 100 °C (table temperature) with a GPC of 0.125 nm/cycle determined on silicon wafer as also described in previous report [43], and the thickness of the SnO_2 layer was 50 nm in this study. Following SnO_2, the ITO was sputtered in the AJA sputter tool to reach 70–80 nm and a Ag grid with thickness of 300 nm was evaporated on the cells as the top electrode. Finally, about 100 nm thick MgF_2 was evaporated on top of the ITO as an anti-reflective coating.

4.2. Spectroscopic ellipsometry

To record the growth per cycle during the ALD-process of NiO films which were deposited on c-Si (100) substrates, in-situ spectroscopic ellipsometry (VIS Ellipsometer M200, J.A. Woolllam Co, with a range of 1.2–5.0 eV) was used. On a Woollam mapping stage (1.24–3.35 eV) the uniformity was determined of the optimized ALD-process, on a 200 mm diameter Si-wafer using two Tauc-Lorentz oscillators to model the NiO films, similar to our previous report [44].

4.3. X-ray photoelectron spectroscopy

Chemical composition of the films was determined by X-ray photoelectron spectroscopy (XPS) using a Thermo Scientific Kα1066 spectrometer. This system utilizes Kα X-rays (1486.6 eV). For depth profile of the films, 500 eV Ar^+ ion sputtering was used, with etching step of 10 s to remove the surface contaminant. To avoid possible peak shifts due to charging, the binding energies of the XPS spectra were corrected by setting the maximum of the adventitious carbon peak in the C1s spectra to 284.4 eV. The assignment of the peaks relied on several literature references. [45–47].

4.4. Current density-Voltage measurement

Measurement was carried out with a Neonsee solar simulator. The sample holder had a temperature control set point at 23 °C to reach sample temperature of 25 °C. The scan rate was 133 mV/s.

4.5. External quantum efficiency

EQE was measured with a commercial setup from Rera Solutions. A Si reference cell from Thorlabs was used to calibrate the wavelengths from 300 nm to 1090 nm and a Ge reference cell for the wavelengths from 1100 nm to 1200 nm.

4.6. Scanning electron microscopy

SEM micrographs of the perovskite top view were captured using FEI NovaNanoLab 600i, used with a 5 kV electron beam.

4.7. X-ray diffraction

XRD patterns of perovskite layer with protective TOPO (tri-octylphosphine oxide) on top were recorded by a Bruker 2D PHASER using Cu Kα ($\lambda = 1.54$ Å) radiation. An increment step size of 0.05° was used between 10 and 40°.

4.8. Ultraviolet photoelectron spectroscopy (UPS) measurement

The measurement was done with an EscaLab II system using -6V bias and the 21.22eV HeI line. The layers were briefly exposed to air prior to the measurement.

4.9. Transmission electron microscopy

A cross-sectional TEM lamella was obtained using a standard Focused Ion Beam (FIB) lift-out procedure. The subsequent TEM studies were performed using a probe-corrected JEOL ARM 200F, operated at 200 kV, equipped with a 100 mm^2 Centurio SDD EDX detector.

4.10. Electrostatic force microscopy

Electrostatic force microscopy was performed with a Veeco Dimension AFM using OMCL-AC240TM-B2 Pt/Al coated atomic force microscopy (AFM) tips. EFM was performed with AM-feedback using Lift Mode for the EFM signal after obtaining topography using AFM in tapping mode. Measurements where performed in ambient conditions at room temperature. The sample was grounded during measurements and the bias (DC + AC) applied to the tip.

CRediT authorship contribution statement

Nga Phung: Writing – review & editing, Writing – original draft, Visualization, Investigation. **Dong Zhang:** Writing – review & editing, Investigation, Conceptualization. **Cristian van Helvoirt:** Writing – review & editing, Investigation. **Michael Verhage:** Writing – review & editing, Investigation. **Marcel Verheijen:** Writing – review & editing, Investigation. **Valerio Zardetto:** Writing – review & editing, Investigation. **Frennie Bens:** Writing – review & editing, Investigation. **Christ H.L. Weijtens:** Investigation. **L.J (Bart) Geerligs:** Investigation, Funding acquisition, Writing – review & editing. **W.M.M. Kessels:** Writing – review & editing, Funding acquisition. **Bart Macco:** Writing – review & editing, Investigation, Funding acquisition. **Mariadriana Creatore:** Writing – review & editing, Supervision, Funding acquisition, Conceptualization.

Declaration of competing interest

The authors declare that they have no known competing financial interests or personal relationships that could have appeared to influence the work reported in this paper.

Data availability

Data will be made available on request.

Acknowledgements

The authors acknowledge the technical support of Caspar van Bommel, Joris Meulendijks and Janneke Zeebregts at TU/e. The authors thank Dr. Beatriz Barcones Campo (TU/e) for preparing the TEM sample using FIB, and Dr. Wim Arnold-Bik at DIFFER for performing RBS measurement. The authors thank Bruno Pinto Branco (TU/e) with the perovskite deposition. Solliance and the Dutch province of Noord-Brabant are acknowledged for funding the TEM facility. This work is supported by the Top consortia for Knowledge and Innovation (TKI) Solar Energy program "PERCspective" (TEUE119005) of the Ministry of Economic Affairs of The Netherlands. M.C. acknowledges the NWO Aspasia program.

Appendix A. Supplementary data

Supplementary data to this article can be found online at https://doi.org/10.1016/j.solmat.2023.112498.

References

[1] C. Kamaraki, M.T. Klug, T. Green, L. Miranda Perez, C. Case, Perovskite/silicon tandem photovoltaics: technological disruption without business disruption, Appl. Phys. Lett. 119 (2021), 070501, https://doi.org/10.1063/5.0054086.
[2] Z. Li, Y. Zhao, X. Wang, Y. Sun, Z. Zhao, Y. Li, H. Zhou, Q. Chen, Cost analysis of perovskite tandem photovoltaics, Joule 2 (2018) 1559–1572, https://doi.org/10.1016/j.joule.2018.05.001.
[3] E. Bellini, KAUST Claims 33.7% Efficiency for Perovskite/silicon Tandem Solar Cell, PVMagazine, 2023. https://www.pv-magazine.com/2023/05/30/kaust-claims-33-7-efficiency-for-perovskite-silicon-tandem-solar-cell/.
[4] F. Fu, J. Li, T.C. Yang, H. Liang, A. Faes, Q. Jeangros, C. Ballif, Y. Hou, Monolithic perovskite-silicon tandem solar cells: from the lab to fab? Adv. Mater. 34 (2022) 2106540. https://doi.org/10.1002/adma.202106540.
[5] K. Sveinbjörnsson, B. Li, S. Mariotti, E. Jarzembowski, L. Kegelmann, A. Wirtz, F. Frühauf, A. Weihrauch, R. Niemann, L. Korte, F. Fertig, J.W. Müller, S. Albrecht, Monolithic perovskite/silicon tandem solar cell with 28.7% efficiency using industrial silicon bottom cells, ACS Energy Lett. 7 (2022) 2654–2656, https://doi.org/10.1021/acsenergylett.2c01358.
[6] Z. Ying, Z. Yang, J. Zheng, H. Wei, L. Chen, C. Xiao, J. Sun, C. Shou, G. Qin, J. Sheng, Y. Zeng, B. Yan, X. Yang, J. Ye, Monolithic perovskite/black-silicon tandems based on tunnel oxide passivated contacts, Joule 6 (2022) 2644–2661, https://doi.org/10.1016/j.joule.2022.09.006.
[7] Z. Ying, X. Yang, J. Zheng, J. Sun, J. Xiu, Y. Zhu, X. Wang, Y. Chen, X. Li, J. Sheng, C. Shou, Y. Zeng, H. Pan, J. Ye, Z. He, Bathocuproine:Ag complex functionalized tunneling junction for efficient monolithic perovskite/TOPCon silicon tandem solar cell, Sol. RRL 6 (2022), 2200793, https://doi.org/10.1002/solr.202200793.
[8] S. Mariotti, K. Jäger, M. Diederich, M. Sophie Härtel, B. Li, K. Sveinbjörnsson, S. Kajari-Schröder, R. Peibst, S. Albrecht, L. Korte, T. Wietler, Monolithic perovskite/silicon tandem solar cells fabricated using industrial p-type POLO/PERC silicon bottom cell technology, Sol. RRL (2022), https://doi.org/10.1002/solr.202101066.
[9] J. Zheng, H. Mehrvarz, F.-J. Ma, C.F.J. Lau, M.A. Green, S. Huang, A.W.Y. Ho-Baillie, 21.8% efficient monolithic perovskite/homo-junction-silicon tandem solar cell on 16 cm^2, ACS Energy Lett. 3 (2018) 2299–2300, https://doi.org/10.1021/acsenergylett.8b01382.
[10] D. Yan, A. Cuevas, J.I. Michel, C. Zhang, Y. Wan, X. Zhang, J. Bullock, Polysilicon passivated junctions: the next technology for silicon solar cells? Joule 5 (2021) 811–828, https://doi.org/10.1016/j.joule.2021.02.013.
[11] J.P. Mailoa, C.D. Bailie, E.C. Johlin, E.T. Hoke, A.J. Akey, W.H. Nguyen, M. D. McGehee, T. Buonassisi, A 2-terminal perovskite/silicon multijunction solar cell enabled by a silicon tunnel junction, Appl. Phys. Lett. 106 (2015), 121105, https://doi.org/10.1063/1.4914179.
[12] J. Werner, A. Walter, E. Rucavado, S.-J. Moon, D. Sacchetto, M. Rienaecker, R. Peibst, R. Brendel, X. Niquille, S. De Wolf, P. Löper, M. Morales-Masis, S. Nicolay, B. Niesen, C. Ballif, Zinc tin oxide as high-temperature stable recombination layer for mesoscopic perovskite/silicon monolithic tandem solar cells, Appl. Phys. Lett. 109 (2016), 233902, https://doi.org/10.1063/1.4971361.
[13] Y. Wu, D. Yan, J. Peng, T. Duong, Y. Wan, S.P. Phang, H. Shen, N. Wu, C. Barugkin, X. Fu, S. Surve, D. Grant, D. Walter, T.P. White, K.R. Catchpole, K.J. Weber, Monolithic perovskite/silicon-homojunction tandem solar cell with over 22% efficiency, Energy Environ. Sci. 10 (2017) 2472–2479, https://doi.org/10.1039/c7ee02288c.
[14] J. Zheng, C.F.J. Lau, H. Mehrvarz, F.J. Ma, Y. Jiang, X. Deng, A. Soeriyadi, J. Kim, M. Zhang, L. Hu, X. Cui, D.S. Lee, J. Bing, Y. Cho, C. Chen, M.A. Green, S. Huang, A.

W.Y. Ho-Baillie, Large area efficient interface layer free monolithic perovskite/homo-junction-silicon tandem solar cell with over 20% efficiency, Energy Environ. Sci. 11 (2018) 2432–2443, https://doi.org/10.1039/c8ee00689j.
[15] H. Shen, S.T. Omelchenko, D.A. Jacobs, S. Yalamanchili, Y. Wan, D. Yan, P. Phang, T. Duong, Y. Wu, Y. Yin, C. Samundsett, J. Peng, N. Wu, T.P. White, G. G. Andersson, N.S. Lewis, K.R. Catchpole, In situ recombination junction between p-Si and TiO_2 enables high-efficiency monolithic perovskite/Si tandem cells, Sci. Adv. 4 (2018), https://doi.org/10.1126/sciadv.aau9711.
[16] R.L.Z. Hoye, K.A. Bush, F. Oviedo, S.E. Sofia, M. Thway, X. Li, Z. Liu, J. Jean, J. P. Mailoa, A. Osherov, F. Lin, A.F. Palmstrom, V. Bulovic, M.D. McGehee, I. M. Peters, T. Buonassisi, Developing a robust recombination contact to realize monolithic perovskite tandems with industrially common p-type silicon solar cells, IEEE J. Photovoltaics 8 (2018) 1023–1028, https://doi.org/10.1109/JPHOTOV.2018.2820509.
[17] J. Zheng, H. Mehrvarz, C. Liao, J. Bing, X. Cui, Y. Li, V.R. Gonçales, C.F.J. Lau, D. S. Lee, Y. Li, M. Zhang, J. Kim, Y. Cho, L.G. Caro, S. Tang, C. Chen, S. Huang, A.W. Y. Ho-Baillie, Large-area 23%-efficient monolithic perovskite/homojunction-silicon tandem solar cell with enhanced UV stability using down-shifting material, ACS Energy Lett. 4 (2019) 2623–2631, https://doi.org/10.1021/acsenergylett.9b01783.
[18] C.U. Kim, J.C. Yu, E.D. Jung, I.Y. Choi, W. Park, H. Lee, I. Kim, D.-K. Lee, K. K. Hong, M.H. Song, K.J. Choi, Optimization of device design for low cost and high efficiency planar monolithic perovskite/silicon tandem solar cells, Nano Energy 60 (2019) 213–221, https://doi.org/10.1016/j.nanoen.2019.03.056.
[19] J. Hyun, K.M. Yeom, H.E. Lee, D. Kim, H.-S. Lee, J.H. Noh, Y. Kang, Efficient n-i-p monolithic perovskite/silicon tandem solar cells with tin oxide via a chemical bath deposition method, Energies 14 (2021) 7614, https://doi.org/10.3390/en14227614.
[20] J.Y. Hyun, K.M. Yeom, S.-W. Lee, S. Bae, D. Choi, H. Song, D. Kang, J.-K. Hwang, W. Lee, S. Lee, Y. Kang, H.-S. Lee, J.H. Noh, D. Kim, Perovskite/silicon tandem solar cells with a V_{OC} of 1784 mV based on an industrially feasible 25 cm^2 TOPCon silicon cell, ACS Appl. Energy Mater. 5 (2022) 5449–5456, https://doi.org/10.1021/acsaem.1c02796.
[21] M. De Bastiani, A.S. Subbiah, E. Aydin, F.H. Isikgor, T.G. Allen, S. De Wolf, Recombination junctions for efficient monolithic perovskite-based tandem solar cells: physical principles, properties, processing and prospects, Mater. Horiz. 7 (2020) 2791–2809, https://doi.org/10.1039/D0MH00990C.
[22] P. Tockhorn, J. Sutter, A. Cruz, P. Wagner, K. Jäger, D. Yoo, F. Lang, M. Grischek, B. Li, J. Li, Nano-optical designs for high-efficiency monolithic perovskite–silicon tandem solar cells, Nat. Nanotechnol. (2022) 1–8, https://doi.org/10.5442/ND000009.
[23] A. Al-Ashouri, E. Köhnen, B. Li, A. Magomedov, H. Hempel, P. Caprioglio, J. A. Márquez, A.B. Morales Vilches, E. Kasparavicius, J.A. Smith, N. Phung, D. Menzel, M. Grischek, L. Kegelmann, D. Skroblin, C. Gollwitzer, T. Malinauskas, M. Jošt, G. Matič, B. Rech, R. Schlatmann, M. Topič, L. Korte, A. Abate, B. Stannowski, D. Neher, M. Stolterfoht, T. Unold, V. Getautis, S. Albrecht, Monolithic perovskite/silicon tandem solar cell with >29% efficiency by enhanced hole extraction, Science 80 (370) (2020) 1300–1309, https://doi.org/10.1126/science.abd4016.
[24] A. Al-Ashouri, A. Magomedov, M. Roß, M. Jošt, M. Talaikis, G. Chistiakova, T. Bertram, J.A. Márquez, E. Köhnen, E. Kasparavičius, S. Levcenco, L. Gil-Escrig, C.J. Hages, R. Schlatmann, B. Rech, T. Malinauskas, T. Unold, C.A. Kaufmann, L. Korte, G. Niaura, V. Getautis, S. Albrecht, Conformal monolayer contacts with lossless interfaces for perovskite single junction and monolithic tandem solar cells, Energy Environ. Sci. 12 (2019) 3356–3369, https://doi.org/10.1039/C9EE02268F.
[25] M. Chockalingam, N. Darwish, G. Le Saux, J.J. Gooding, Importance of the indium tin oxide substrate on the quality of self-assembled monolayers formed from organophosphonic acids, Langmuir 27 (2011) 2545–2552, https://doi.org/10.1021/la104464w.
[26] M.D. Losego, J.T. Guske, A. Efremenko, J.-P. Maria, S. Franzen, Characterizing the molecular order of phosphonic acid self-assembled monolayers on indium tin oxide surfaces, Langmuir 27 (2011) 11883–11888, https://doi.org/10.1021/la201161q.
[27] N. Phung, M. Verheijen, A. Todinova, K. Datta, M. Verhage, A. Al-Ashouri, H. Köbler, X. Li, A. Abate, S. Albrecht, M. Creatore, Enhanced self-assembled monolayer surface coverage by ALD NiO in p-i-n perovskite solar cells, ACS Appl. Mater. Interfaces 14 (2022) 2166–2176, https://doi.org/10.1021/acsami.1c15860.
[28] G. Dingemans, B. Jongbloed, W. Knaepen, D. Pierreux, L. Jdira, H. Terhorst, Merits of batch ALD, ECS Trans. 64 (2014) 35–49, https://doi.org/10.1149/06409.0035ecst.
[29] P. Poodt, D.C. Cameron, E. Dickey, S.M. George, V. Kuznetsov, G.N. Parsons, F. Roozeboom, G. Sundaram, A. Vermeer, Spatial atomic layer deposition: a route towards further industrialization of atomic layer deposition, J. Vac. Sci. Technol. A Vacuum, Surfaces, Film. 30 (2012), 010802, https://doi.org/10.1116/1.3670745.
[30] J.A. Raiford, S.T. Oyakhire, S.F. Bent, Applications of atomic layer deposition and chemical vapor deposition for perovskite solar cells, Energy Environ. Sci. 13 (2020) 1997–2023, https://doi.org/10.1039/D0EE00385A.
[31] A.E.A. Bracesco, C.H. Burgess, A. Todinova, V. Zardetto, D. Koushik, W.M.M. E. Kessels, I. Dogan, C.H.L. Weijtens, S. Veenstra, R. Andriessen, M. Creatore, The chemistry and energetics of the interface between metal halide perovskite and atomic layer deposited metal oxides, J. Vac. Sci. Technol. A. 38 (2020), 063206, https://doi.org/10.1116/6.0000447.
[32] A. Hultqvist, T.J. Jacobsson, S. Svanström, M. Edoff, U.B. Cappel, H. Rensmo, E.M. J. Johansson, G. Boschloo, T. Törndahl, SnOx atomic layer deposition on bare perovskite—an investigation of initial growth dynamics, interface chemistry, and solar cell performance, ACS Appl. Energy Mater. (2021), https://doi.org/10.1021/acsaem.0c02405.
[33] Y. Lin, Y. Firdaus, F.H. Isikgor, M.I. Nugraha, E. Yengel, G.T. Harrison, R. Hallani, A. El-Labban, H. Faber, C. Ma, X. Zheng, A. Subbiah, C.T. Howells, O.M. Bakr, I. McCulloch, S. De Wolf, L. Tsetseris, T.D. Anthopoulos, Self-assembled monolayer enables hole transport layer-free organic solar cells with 18% efficiency and improved operational stability, ACS Energy Lett. 5 (2020) 2935–2944, https://doi.org/10.1021/acsenergylett.0c01421.
[34] L. Li, Y. Wang, X. Wang, R. Lin, X. Luo, Z. Liu, K. Zhou, S. Xiong, Q. Bao, G. Chen, Y. Tian, Y. Deng, K. Xiao, J. Wu, M.I. Saidaminov, H. Lin, C.-Q. Ma, Z. Zhao, Y. Wu, L. Zhang, H. Tan, Flexible all-perovskite tandem solar cells approaching 25% efficiency with molecule-bridged hole-selective contact, Nat. Energy 7 (2022) 708–717, https://doi.org/10.1038/s41560-022-01045-2.
[35] J. Sun, C. Shou, J. Sun, X. Wang, Z. Yang, Y. Chen, J. Wu, W. Yang, H. Long, Z. Ying, X. Yang, J. Sheng, B. Yan, J. Ye, NiOx -seeded self-assembled monolayers as highly hole-selective passivating contacts for efficient inverted perovskite solar cells, Sol. RRL 5 (2021), 2100663, https://doi.org/10.1002/solr.202100663.
[36] K. Datta, J. Wang, D. Zhang, V. Zardetto, W.H.M. Remmerswaal, C.H.L. Weijtens, M.M. Wienk, R.A.J. Janssen, Monolithic all-perovskite tandem solar cells with minimized optical and energetic losses, Adv. Mater. 34 (2022), https://doi.org/10.1002/adma.202110053.
[37] L. Canil, T. Cramer, B. Fraboni, D. Ricciarelli, D. Meggiolaro, A. Singh, M. Liu, M. Rusu, C.M. Wolff, N. Phung, Q. Wang, D. Neher, T. Unold, P. Vivo, A. Gagliardi, F. De Angelis, A. Abate, Tuning halide perovskite energy levels, Energy Environ. Sci. 14 (2021) 1429–1438, https://doi.org/10.1039/D0EE02216K.
[38] D. Otálvaro, T. Veening, G. Brocks, Self-assembled monolayer induced Au(111) and Ag(111) reconstructions: work functions and interface dipole formation, J. Phys. Chem. C 116 (2012) 7826–7837, https://doi.org/10.1021/jp300512k.
[39] J. Zheng, G. Wang, W. Duan, M.A. Mahmud, H. Yi, C. Xu, A. Lambertz, S. Bremner, K. Ding, S. Huang, Monolithic perovskite–perovskite–silicon triple-junction tandem solar cell with an efficiency of over 20%, ACS Energy Lett 7 (2022) 3003–3005. https://doi.org/10.1021/acsenergylett.2c01556.
[40] X. Zhang, W. Qiu, S. Apergi, S. Singh, P. Marchezi, W. Song, C. Sternemann, K. Elkhouly, D. Zhang, A. Aguirre, Minimizing the interface-driven losses in inverted perovskite solar cells and modules, ACS Energy Lett 8 (2023) 2532–2542. https://doi.org/10.1021/acsenergylett.3c00697.
[41] B. Macco, B.W.H. van de Loo, M. Dielen, D.G.J.A. Loeffen, B.B. van Pelt, N. Phung, J. Melskens, M.A. Verheijen, W.M.M. Kessels, Atomic-layer-deposited Al-doped zinc oxide as a passivating conductive contacting layer for n^+-doped surfaces in silicon solar cells, Sol. Energy Mater. Sol. Cells 233 (2021), 111386, https://doi.org/10.1016/j.solmat.2021.111386.
[42] B.W.H. van de Loo, B. Macco, J. Melskens, W. Beyer, W.M.M. Kessels, Silicon surface passivation by transparent conductive zinc oxide, J. Appl. Phys. 125 (2019), 105305, https://doi.org/10.1063/1.5054166.
[43] J. Wang, V. Zardetto, K. Datta, D. Zhang, M.M. Wienk, R.A.J. Janssen, 16.8% Monolithic all-perovskite triple-junction solar cells via a universal two-step solution process, Nat. Commun. 11 (2020) 1–10, https://doi.org/10.1038/s41467-020-19062-8.
[44] D. Koushik, M. Jošt, A. Dučinskas, C. Burgess, V. Zardetto, C. Weijtens, M. A. Verheijen, W.M.M. Kessels, S. Albrecht, M. Creatore, Plasma-assisted atomic layer deposition of nickel oxide as hole transport layer for hybrid perovskite solar cells, J. Mater. Chem. C 7 (2019) 12532–12543, https://doi.org/10.1039/c9tc04282b.
[45] J.F. Moulder, W.F. Stickle, S. P.E, K.D. Bomben, Handbook of X-Tay Photoelectron Spectroscopy, Perkin-Elmer Corp., 1992.
[46] M.C. Biesinger, B.P. Payne, L.W.M. Lau, A. Gerson, R.S.C. Smart, X-ray photoelectron spectroscopic chemical state Quantification of mixed nickel metal, oxide and hydroxide systems, Surf. Interface Anal. 41 (2009) 324–332, https://doi.org/10.1002/sia.3026.
[47] Y.A. Teterin, K.I. Maslakov, E.N. Murav'ev, A.Y. Teterin, N.A. Bulychev, B. B. Meshkov, D.S. Stepnov, X-Ray photoelectron spectroscopy study of indium tin mixed oxides on the surface of silicate glass, Inorg. Mater. 56 (2020) 482–493, https://doi.org/10.1134/S0020168520050131.